

# PATCH-BASED SPARSE REPRESENTATION FOR BACTERIAL DETECTION

A. K. Eldaly<sup>(1),(2)</sup>, Y. Altmann<sup>(1)†</sup>, A. Akram<sup>(2)</sup>, A. Perperidis<sup>(1),(2)\*</sup>, K. Dhaliwal<sup>(2)</sup>, S. McLaughlin<sup>(1)</sup>

<sup>(1)</sup>School of Engineering and Physical Sciences, Heriot-Watt University, Edinburgh, United Kingdom

<sup>(2)</sup>The Queen’s Medical Research Institute, The University of Edinburgh, Edinburgh, United Kingdom

## ABSTRACT

In this paper, we propose a supervised approach for bacterial detection in optical endomicroscopy images. This approach splits each image into a set of overlapping patches and assumes that observed intensities are linear combinations of the actual intensity values associated with background image structures, corrupted by additive Gaussian noise and potentially by a sparse outlier term modelling anomalies (which are considered to be candidate bacteria). The actual intensity term representing background structures is modelled as a linear combination of a few atoms drawn from a dictionary which is learned from bacteria-free data and then fixed while analyzing new images. The bacteria detection task is formulated as a minimization problem and an Alternating Direction Method of Multipliers (ADMM) is then used to estimate the unknown parameters. Simulations conducted using two *ex vivo* lung datasets show good detection and correlation performance between bacteria counts identified by a trained clinician and those of the proposed method.

**Index Terms**— Sparse representation, anomaly detection, bacteria detection, Optical microscopy, patch-based methods, ADMM.

## 1. INTRODUCTION

Pneumonia is characterized by a host inflammatory response to a pathogenic infectious burden in the distal lung and is usually caused by bacterial infection [1]. However, accurate quantitative diagnosis and monitoring of suspected pneumonia is a challenging task with currently available imaging/diagnostic tools [2]. Optical endomicroscopy (OEM) is a popular method for *in vivo* imaging of the distal lung, and has recently gained prominence in investigating the presence of bacteria using targeted smartprobe [1]. Smartprobes are specialized molecular agents introduced in the imaging area to make the bacteria fluoresce.

Outlier/anomaly detection problems can usually be addressed using unsupervised or supervised methods [3]. In unsupervised approaches, the objects/anomalies to be detected are learned from the data by fitting them with suitable distributions without using explicitly-provided labels [4–11]. On the other hand, considering supervised approaches, the dataset is usually divided into training and testing sets. In the training phase, a model is trained by pairing inputs with their expected outputs, which are also known as the ground truth. The trained model can then be used to estimate the output of the test dataset [12–15].

In this work, we investigate the performance of a supervised approach for bacterial detection in datasets of OEM lung images [16–21]. The main contributions of this work are threefold. First, we formulate the problem of simultaneous bacteria detection and

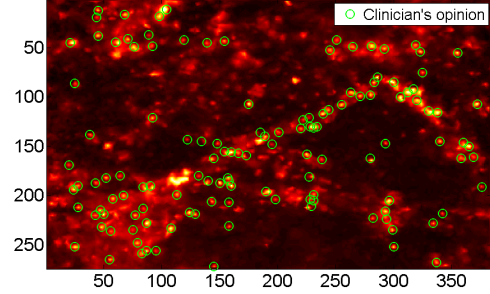


**Fig. 1:** An OEM image with bacteria shown within circles annotated by a trained clinician.

background estimation as a (robust) sparse coding problem and use an ADMM algorithm to solve the bacteria detection problem. To the best of our knowledge, it is the first time this problem is addressed by a sparse representation approach. Second, we provide simulations using real datasets, whereby we investigate different bacterial concentrations including control cases in which no bacteria are present, and different SmartProbes that cause weak and strong bacteria fluorescence. Third, we compare the results of the proposed model with bacteria annotations performed by a trained clinician and three widely used spot-detection algorithms, using both dot-annotation and count-annotation methods.

## 2. OUTLIER DETECTION FORMULATION

Figure 1 shows an example of an OEM image with bacteria shown within circles that are annotated by a trained clinician. We can observe that bacteria appear as high intensity dots in the image in addition to as bright as background structures representing elastin and collagen, making the differentiation of bacteria a quite challenging task. The problem of bacteria detection is formulated such that, given a test image  $\mathcal{I} \in \mathbb{R}^{m \times n}$ , a data matrix  $\mathbf{Y} \in \mathbb{R}^{P \times L}$  is formed by splitting the image into a set of  $L$  overlapping square patches containing  $P = N_p^2$  pixels. These patches are vectorized and finally gathered in  $\mathbf{Y} = [\mathbf{y}_1, \mathbf{y}_2, \dots, \mathbf{y}_L]$ . The data matrix  $\mathbf{Y}$  can then be well approximated by a sparse linear model, excluding a small number of pixels - the outliers - which significantly deviate from this model. The collection  $\mathbf{Y}$  is described as follows

$$\mathbf{Y} = \mathbf{D}\Psi + \mathbf{R} + \mathbf{W}, \quad (1)$$

where  $\mathbf{D} \in \mathbb{R}^{P \times K}$  is a dictionary assumed to be known,  $\Psi \in \mathbb{R}^{K \times L}$  is the sparse coefficient matrix,  $\mathbf{R} \in \mathbb{R}^{P \times L}$  has few non-zero elements that represents sparse deviations from the linear model  $\mathbf{D}\Psi$  representing background image structures, and  $\mathbf{W} \in \mathbb{R}^{P \times K}$  is a low-energy noise component, which is assumed to be independent and identically distributed (i.i.d.) Gaussian.

The primary objective here is to estimate the outlier matrix  $\mathbf{R}$  in Eq. (1), given that the sparse coefficients in  $\Psi$  are also unknown. Thus we propose to estimate jointly  $(\mathbf{R}, \Psi)$  from the observation

<sup>†</sup>Part of this work was supported by the Royal Academy of Engineering through the research fellowship scheme (RF201617/16/31).

\*Part of this work was supported by the EPSRC via grant EP/K03197X/1.

matrix  $\mathbf{Y}$ . To solve this problem, we propose an optimization-based method to estimate the unknown parameters.

### 3. PROPOSED MODEL

The recovery of  $\mathbf{R}$  and  $\Psi$  in Eq.(1) is formulated as the following unconstrained minimization problem

$$\underset{\Psi, \mathbf{R}}{\text{minimize}} \quad \frac{1}{2} \|\mathbf{Y} - \mathbf{D}\Psi - \mathbf{R}\|_F^2 + \alpha \|\Psi\|_{1,1} + \beta \|\mathbf{R}\|_{1,1}, \quad (2)$$

where  $\Psi = [\Psi_1, \dots, \Psi_K]^T$ ,  $\|\Psi\|_{1,1} = \sum_k \|\Psi(k, :)\|_1$ , similarly  $\mathbf{R} = [\mathbf{R}_1, \dots, \mathbf{R}_P]^T$ ,  $\|\mathbf{R}\|_{1,1} = \sum_p \|\mathbf{R}(p, :)\|_1$ , and  $\alpha$  and  $\beta$  are two positive scalar parameters controlling the degree of sparsity of  $\Psi$  and  $\mathbf{R}$  respectively. Problem (2) encourages a solution in which  $\Psi$  is sparse. However, for the outliers that cannot be represented exclusively by  $\mathbf{D}$ , it permits non-zero entries in  $\mathbf{R}$ .

The optimization problem in Eq. (2), although convex, cannot be solved using standard gradient-based methods due to the non-smooth terms. The core idea is to convert this unconstrained minimization problem into another constrained one by the application of a variable splitting operation (see Eq. (3) below). Finally, the obtained constrained problem is solved with using ADMM [19, 22, 23]. By a careful choice of the new variables, the initial problem is converted into a sequence of much simpler problems, which can be solved iteratively. To solve the problem depicted in Eq. (3), we introduce a new variable  $\mathbf{Z}$  for the regularization function in  $\Psi$  in order to decouple it from the data fidelity term. Therefore, the constrained version of problem (2) can be written as follows

$$\underset{\Psi, \mathbf{R}}{\text{minimize}} \quad \frac{1}{2} \|\mathbf{Y} - \mathbf{D}\Psi - \mathbf{R}\|_F^2 + \alpha \|\mathbf{Z}\|_{1,1} + \beta \|\mathbf{R}\|_{1,1},$$

subject to  $\mathbf{Z} = \Psi.$  (3)

The augmented Lagrangian corresponding to the problem in Eq. (3) can be written as  $\mathcal{L}(\Psi, \mathbf{R}, \mathbf{Z}, \mathbf{M}) = \frac{1}{2} \|\mathbf{Y} - \mathbf{D}\Psi - \mathbf{R}\|_F^2 + \alpha \|\mathbf{Z}\|_{1,1} + \beta \|\mathbf{R}\|_{1,1} + \frac{\mu}{2} \|\mathbf{Z} - \Psi - \mathbf{M}\|_F^2$ , where  $\mathbf{M}$  is the set of Lagrange multiplier corresponding to the splitting, and  $\mu > 0$  is a constant. The ADMM algorithm using to solve Eq. (3) (also Eq. (2)) is shown in Algorithm 1. During each step of this iterative scheme,  $\mathcal{L}$  is optimized with respect to  $\Psi$  (step 2),  $\mathbf{R}$  (step 3) and  $\mathbf{Z}$  (step 4), and then the Lagrange multipliers are updated (step 5).

---

#### Algorithm 1 Sparse coding with Bacterial Detection - Version I

---

- 0: set  $k = 0$ , choose  $\mu > 0$ ,  $\Psi^{(0)}$ ,  $\mathbf{R}^{(0)}$ ,  $\mathbf{Z}^{(0)}$ , and  $\mathbf{M}^{(0)}$
  - 1: **repeat** ( $k \leftarrow k + 1$ )
  - 2:  $\Psi^{(k+1)} \leftarrow \text{minimize}_{\Psi} \mathcal{L}(\Psi, \mathbf{R}^k, \mathbf{Z}^k, \mathbf{M}^k)$
  - 3:  $\mathbf{R}^{(k+1)} \leftarrow \text{minimize}_{\mathbf{R}} \mathcal{L}(\Psi^{k+1}, \mathbf{R}, \mathbf{Z}^k, \mathbf{M}^k)$
  - 4:  $\mathbf{Z}^{(k+1)} \leftarrow \text{minimize}_{\mathbf{Z}} \mathcal{L}(\Psi^{k+1}, \mathbf{R}^{k+1}, \mathbf{Z}, \mathbf{M}^k)$
  - 5: **Update**  $\mathbf{M}$  :  $\mathbf{M}^{(k+1)} \leftarrow \mathbf{M}^{(k)} - (\mathbf{Z}^{(k+1)} - \Psi^{(k+1)})$
  - 6: **until** some stopping criterion is satisfied.
- 

Solving the minimization problems in Algorithm 1 leads to Algorithm 2, where  $\Upsilon = \mathbf{Y} - \mathbf{R}$ ,  $\mathbf{F} = \mathbf{Z} + \mathbf{M}$  and *soft* is the soft thresholding function [24]. The parameter  $\mu > 0$  is updated within the algorithm to keep the primal and dual residual norms within a factor of 10 of one another. The stopping criterion we use is  $(\|\mathbf{Z}^{(k)} - \Psi^{(k)}\|_F + \mu \|\mathbf{M}^{(k)} - \mathbf{M}^{(k+\rho)}\|_F) \leq \epsilon$ , which is the sum of the primal and dual residuals, where  $\epsilon = \sqrt{P \times L} \times 10^{-6}$  [19, 22].

## 4. EXPERIMENTAL RESULTS

### 4.1. Datasets

The proposed algorithm is assessed using two datasets of *ex vivo* ventilated whole ovine lungs with bacteria present. Dataset I contains seven videos assessing a combination of fluorescent dyes

---

#### Algorithm 2 Sparse coding with Bacterial Detection - Version II

---

- 1: set  $k = 0$ , choose  $\mu > 0$ ,  $\Psi^{(0)}$ ,  $\mathbf{R}^{(0)}$ ,  $\mathbf{Z}^{(0)}$ , and  $\mathbf{M}^{(0)}$
  - 2: **repeat** ( $k \leftarrow k + 1$ )
  - 3:  $\Psi^{(k+1)} \leftarrow (\mathbf{D}^T \mathbf{D} + \mu^{(k)} \mathbf{I})^{-1} (\mathbf{D}^T \Upsilon^{(k)} + \mu^{(k)} \mathbf{F}^{(k)})$ ,
  - 4:  $\mathbf{R}^{(k+1)} \leftarrow \text{soft}(\mathbf{Y} - \mathbf{D}\Psi^{(k+1)}, \beta)$ ,
  - 5:  $\mathbf{Z}^{(k+1)} \leftarrow \text{soft}(\Psi^{(k+1)} - \mathbf{M}^{(k)}, \frac{\alpha}{\mu})$ ,
  - 6:  $\mathbf{M}^{(k+1)} \leftarrow \mathbf{M}^{(k)} - (\mathbf{Z}^{(k+1)} - \Psi^{(k+1)})$
  - 7: **until** some stopping criterion is satisfied.
- 

Table 1: Description of dataset I.

Video	# of frames	Bacteria concent. (OD)	Fluorophore	Bacteria
1	26	2	PKH	MSSA
2	19			
3	13		SmartProbe	PA
4	32			MSSA
5	19			
6	12	NA	NA	Control
7	12			

(SmartProbes) and bacterial types, including control segments. It contains (i) three videos of ovine lungs instilled with *Methicillin-sensitive Staphylococcus aureus* (MSSA) stained with a commercially available laboratory dye (PKH67, Sigma-Aldrich), a highly fluorescent cell membrane dye, (ii) two videos of ovine lungs instilled with bacteria (gram-positive MSSA and gram-negative *Pseudomonas* PA3284) stained in situ with an in-house bacterial detection SmartProbe [1], and (iii) two videos of ovine lungs without the presence of any bacteria. Videos 1 to 5 are instilled with a single concentration of bacteria, equivalent to Optical Density (OD595nm) of 2.

Dataset II contains four videos, each with an increasing bacterial concentration (OD595nm 0.004, 0.04, 0.4, 4), all labelled with an in-house bacterial detection SmartProbe. This dataset is considered to make sure that as the concentration increases, the counts of the clinician and of the algorithm also increase. Tables 1 and 2 summarise the details of Datasets I and II respectively.

Table 2: Description of dataset II.

Video	# of frames	Bacteria concent. (OD)	Fluorophore	Bacteria
1	14	0.004	SmartProbe	PA
2	14	0.04		
3	15	0.4		
4	15	4		

The Cellvizio fibred confocal OEM imaging platform (Mauna Kea Technologies, Paris, France) [16, 17] is used to acquire all data in this study. Image sequences of size  $274 \times 384$  pixels ( $306\mu\text{m} \times 429\mu\text{m}$ ) are captured at 12 frames per second. Representative frames are selected from each of the video sequences are chosen by a trained clinician. These comprise 133 frames for Dataset I, and 58 frames for Dataset II as described in Tables 1 and 2 respectively. In each frame, a trained clinician marked the coordinates of phenomena that are thought with high confidence to be bacteria. Ambiguous points are ignored.

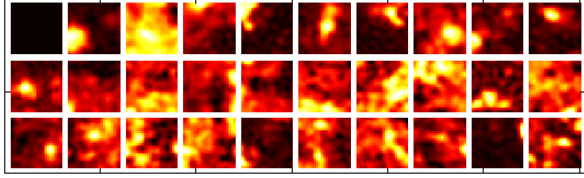


Fig. 2: Example of dictionary atoms learned from Dataset I.

#### 4.2. Dictionary Learning for Bacterial Detection

Each dataset is split into training and testing phases. In the training phase, one dictionary is learned for each dataset from its corresponding videos; namely  $\mathbf{D}_1$  for Dataset I and  $\mathbf{D}_2$  for Dataset II. Every set of frames in each video has a certain elastin and collagen pattern. Hence, one frame from each set is chosen as a representative. This yielded 12 frames from Dataset I and 17 frames from Dataset II. Features are then extracted from each training frame by dividing it into square overlapping patches of fixed size. In this work, we employed a  $27 \times 27$  window size with 50% overlap. The patches that are annotated by the clinician as containing bacteria are then excluded from the training dataset (see Fig. 1). The remaining bacteria-free patches are vectorised and gathered in the training matrix  $\mathbf{Y}_{tr} \in \mathbb{R}^{729 \times 3553}$  for Dataset I and  $\mathbf{Y}_{tr} \in \mathbb{R}^{729 \times 7087}$  Dataset II. The method of optimal directions (MOD) dictionary learning method [25] is then applied to train the dictionaries. The K-SVD algorithm [26] is also investigated but provided similar results to MOD, thus the results are not reported here. Figure 2 shows 30 dictionary atoms learned for a selection of frames from Datasets I.

#### 4.3. Algorithm evaluation

In the testing phase, after the dictionaries have been learned, Algorithm 2 is run for each of the remaining 111 and 41 frames for Dataset I and II respectively, yielding the estimated outlier matrix  $\hat{\mathbf{R}}$  for each frame. The final outlier image is then reconstructed using these overlapping patches by averaging their intensities. The outlier image is then normalized to  $[0, 1]$  range and thresholded (by  $\ell_d$ ), while pixels that exceed this threshold value are counted as a potential bacteria. Since each bacterium corresponds to a set of connected pixels, each group of connected detections is counted as a single detection. The estimated number of bacteria is thus the number of estimated groups and their positions are computed using the barycenter of each region.

Due to the unbalance of this two-class problem (absence/ existence of bacteria), we consider precision-recall curves to assess the bacteria detection performance, in which the reference is the set of annotations from the clinicians. Precision-recall curves are plots of precision versus recall at different cut-off thresholds (different  $\ell_d$ ) for the resulting outlier amplitude image. The precision and the recall can be calculated as  $\text{Precision} = \frac{\text{TP}}{\text{TP} + \text{FP}}$ ,  $\text{Recall} = \frac{\text{FP}}{\text{FP} + \text{FN}}$  respectively, where TP, FN, and FP refer to the number of true positives, false negatives, and false positives respectively. Given the pixel locations where a bacterium has been annotated by the clinician, we defined a disk of radius  $r = 10$  pixels [27], and we consider that any detection that is present within the disk as a match (TP); any detection outside any of the disks as FP; and any clinician's annotation that does not match with any of the algorithm detection as FN.

We test different parameters for evaluating the performance of the proposed algorithm. First, we fix the regularization parameter  $\alpha$  corresponding to the sparse representation matrix  $\Psi$  to  $\alpha = 1 \times 10^{-5}$ , and vary the outlier regularization parameter ( $\beta$ ). Second, we investigate the impact of the number of atoms ( $K$ ) within the learned dictionary. Finally we vary the outlier amplitude image threshold ( $\ell_d$ ) between 0 and 1, and construct the precision-

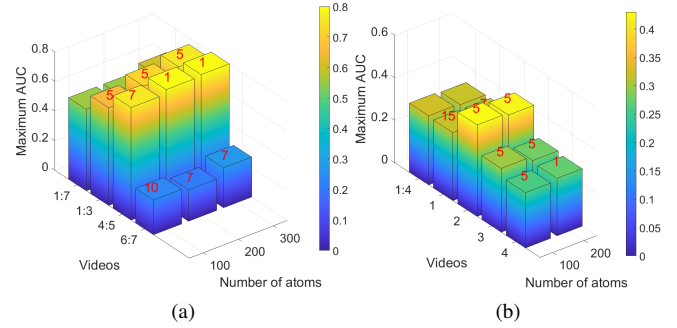


Fig. 3: Plot of maximum achieved AUC reported for Dataset I in (a) and II in (b). The corresponding values of  $\beta$  are provided above each bar in red.

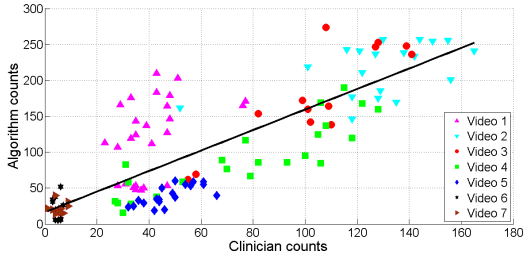
recall curves accordingly. Statistical comparison of bacterial counts (count-annotation) and detections (dot-annotation) performed by the trained clinicians and the algorithm output is then considered after choosing the best combination of the parameters described above.

#### 4.4. Results and Discussion

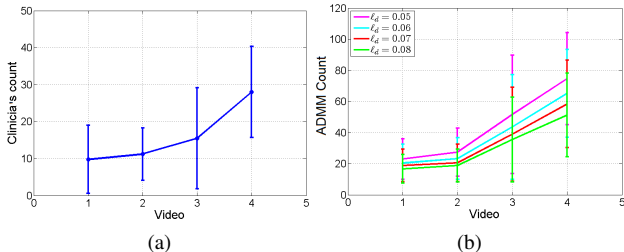
**Dot-annotation effect:** Figure 3(a) shows a plot of different smartprobes (represented by video ranges) versus different numbers of dictionary atoms and the maximum achieved area under precision-recall curve (AUC). It can be noted that the bacteria detection performance is enhanced when increasing the number of dictionary atoms. Although a strong smartprobe which produces high fluorescence signals is used for videos 1:3, the reported AUC is close to that for videos 3:4, for which a weaker smartprobe is used. This is because videos 4 and 5 have less elastin and collagen structures, and hence there is lower probability of getting false positive detections. Regarding the control cases (videos 6 and 7), it can be observed that the optimal regularization parameter  $\beta$  (printed in red on top of each bar) is always higher than that of the bacteria stained videos (videos 1:3 and 4:5), which in turn promotes more outlier sparseness and hence fewer counts. Moreover, the AUCs of these videos are lower than those of videos 1:3 and 4:5, as they are not stained by fluorophores and hence makes the fluorescence of bacteria weaker and more difficult to discriminate, stressing the need for SmartProbes for bacterial detection. We also noticed that there a broad range of outlier regularization parameters provides very similar precision-recall curves, and the results are not extremely sensitive to the value of  $\beta$ .

Figure 3(b), on the other hand, shows a plot of the four concentrations (represented by video numbers) versus different numbers of atoms and the maximum achieved AUC. We note that there is not much difference in the achieved maximum AUC for the two tested dictionary atom numbers. We also noticed that there is a broad range of the regularization parameter  $\beta$  values that provides same AUC.

**Count-annotation effect:** For Dataset I, the algorithm counts are compared with the clinician counts in each frame as shown in Fig. 4. This corresponds to precision of 50% and recall of 86.12% that also corresponds to cut-off threshold to the outlier amplitude images of  $\ell_d = 0.07$ . We considered the values of  $\beta$  providing the maximum AUC per each fluorophore. We can observe an almost linear relationship between the clinician counts and algorithm counts, with an empirical linear correlation between the manually and automatically detected anomalies as 0.823. Furthermore, for videos 1, 2 and 3 in which a highly fluorescent SmartProbe is used, and videos 4 and 5 in which an in-house SmartProbe which produces weaker fluorescence signals is used, a similar trend is observed between the numbers of clinician's annotations and the counts provided by our



**Fig. 4:** Plot of clinician bacteria count versus algorithm bacteria count for Dataset I. Dots correspond to frames, and colours correspond to videos.



**Fig. 5:** Mean number of detections per selected frames in videos 1 to 4 of Dataset II and the corresponding standard deviation. (a) clinician’s opinion, (b) proposed method.

algorithm. This also depending on the type of bacteria the samples are stained with. Videos 6 and 7, which are controls, show minimal annotations and counts, which reflects the ability of the algorithm to differentiate bacterial loads from control.

Similarly, for Dataset II, we compared the clinician-algorithm counts for different cut-off thresholds  $\ell_d$ , ranging between  $\ell_d = 0.05$  and  $\ell_d = 0.08$ , which corresponds to total recall of 82.03% to 66.58% and precision of 23.64% to 32.4%, and provided the results in Fig. 5. This corresponds to the counts provided by maximum AUC when different values of  $\beta$  are tested. We can observe that the counts of both the algorithm and the clinician increase as the bacteria concentration increases, which reflects the agreement between the approach considered and the clinician’s annotations.

We can also observe that the algorithm counts are higher than those of the clinician for the two processed datasets, as we expect the algorithm to be able to identify dots that are barely visible to the naked eye. Moreover, the clinician did not annotate ambiguous dots, meaning that a number of these are not chosen. This, along with false positives, is the main reason why the algorithm counts are higher than the clinician counts.

#### 4.5. Comparison with existing approaches

In this subsection, we compare the proposed approach with popular spot-detection methods from the literature, namely the Laplacian of Gaussian (LoG) and its approximation; the difference of Gaussians (DoG) filters [11, 28], and the grey scale opening top-hat filter (GSOTH) [9, 10]. These methods, although simple, have been considered in the literature of spot and blob detection in various applications. In this work, from preliminary trials to optimize performance, the LoG filter is implemented by employing a  $3 \times 3$  kernel of standard deviation of 3 to each frame. Similarly, the DoG filter is implemented by considering the difference of two  $3 \times 3$  Gaussian kernels of standard deviations of 3 and 5 respectively. The GSOTH is employed by first smoothing the input image by a Gaussian kernel to reduce the noise, then by computing the morphological opening of the input image by employing a  $3 \times 3$  flat disc, which achieves the best

**Table 3:** Area under curve measures of the resulting precision-recall curves of the proposed approach and three existing methods. Bold (resp. underlined) represent best (resp. second best) results.

		Sparse coding	LoG	DoG	GSOTH
		AUC			
Dataset I	Videos 1:3	<b>0.754</b>	0.58	0.56	<u>0.749</u>
	4:5	<b>0.8</b>	0.53	0.63	<u>0.786</u>
	6:7	<b>0.27</b>	<u>0.175</u>	0.104	0.172
	<b>Average</b>	<b>0.61</b>	0.43	0.43	<u>0.569</u>
Dataset II	1	<b>0.32</b>	0.142	0.14	<u>0.257</u>
	2	<b>0.43</b>	0.18	0.268	<u>0.322</u>
	3	<b>0.30</b>	0.09	0.116	<u>0.184</u>
	4	<b>0.26</b>	0.136	0.115	<u>0.226</u>
	<b>Average</b>	<b>0.33</b>	0.137	0.16	<u>0.247</u>

detection results and then subtracts the result from the original image. The same post processing steps described earlier (pixel grouping and computation of the barycenters) are also employed. The comparison is conducted in terms of AUC of the resulting precision-recall curves, as well as in terms of computation time.

Table 3 compares the maximum achieved AUC of the proposed algorithm for Datasets I and II with those of the three methods described above. We can observe that the proposed algorithm provides the highest AUC for both Datasets I and II. Although the grey scale opening top-hat filter provides competitive results for videos 1:3 and 4:5 in Dataset I, it fails to identify the control cases as good as the proposed approach. The LoG and the DoG filters, on the other hand, show similar performance.

The average computation times of the four methods are 0.4, 0.11, 0.05 and 0.22 seconds respectively. For the proposed approach, the resulting number of test patches is 468 yielding  $\mathbf{Y} \in \mathbb{R}^{729 \times 468}$ , and the dictionary tested is  $\mathbf{D} \in \mathbb{R}^{729 \times 100}$ . The experiments were conducted on ACER core-i3-2.0 GHz processor laptop with 8 GB RAM. Although the proposed approach provides slightly higher computation time, it crucially brings the benefit of providing higher detection performance with respect to the other three methods.

## 5. CONCLUSION AND FUTURE WORK

In this work, we have demonstrated the performance of a supervised approach for bacterial detection in OEM images of distal lung tissue using targeted SmartProbes. We learned a dictionary for background image structure (elastin, collagen, etc.), which was then used to predict any deviating outliers in testing frames. We have provided simulations on two ovine lung datasets instilled with bacteria, which demonstrated that the estimated bacterial counts correlates with the bacterial counts performed by a clinician and good AUC were achieved. However, precautions should be considered when learning the dictionaries for such problems. While annotating ground truth, it is highly likely that the annotator makes mistakes: they can either falsely annotate a bacterium when it is noise, or simply miss-annotating a bacterium due to their overwhelming numbers in each frame. These types of error are common in any annotation process, but it might have a more severe impact on learning the dictionary since our target objects are ‘dots’ with similar structure. Therefore, wrongly annotated/un-annotated bacteria can provide biased dictionary atoms that cause errors in the estimation process. Current investigations include unsupervised and robust methods for learning the dictionary in the case of absence or unreliability of annotations.

## 6. REFERENCES

- [1] A. R. Akram, N. Avlonitis, T. Craven, M. Vendrell, N. McDonald, E. Scholefield, A. Fisher, P. Corris, C. Haslett, M. Bradley, and K. Dhaliwal, "Structural modifications of the antimicrobial peptide ubiquicidin for pulmonary imaging of bacteria in the alveolar space," *The Lancet*, vol. 387, p. S17, Feb 2016, spring Meeting for Clinician Scientists in Training 2016.
- [2] L. Thiberville, S. Moreno-Swirc, T. Vercauteren, E. Peltier, C. Cavé, and G. Bourg Heckly, "In vivo imaging of the bronchial wall microstructure using fibered confocal fluorescence microscopy," *American journal of respiratory and critical care medicine*, vol. 175, no. 1, pp. 22–31, Jan 2007.
- [3] I. Smal, M. Loog, W. Niessen, and E. Meijering, "Quantitative comparison of spot detection methods in fluorescence microscopy," *IEEE Trans. on Medical Imag.*, vol. 29, no. 2, pp. 282–301, Feb 2010.
- [4] X. Ding, L. He, and L. Carin, "Bayesian robust principal component analysis," *IEEE Trans. on Image Process.*, vol. 20, no. 12, pp. 3419–3430, Dec 2011.
- [5] Y. Altmann, S. McLaughlin, and A. Hero, "Robust linear spectral unmixing using anomaly detection," *IEEE Trans. Comput. Imag.*, vol. 1, no. 2, pp. 74–85, June 2015.
- [6] P. McCool, Y. Altmann, A. Perperidis, and S. McLaughlin, "Robust Markov random field outlier detection and removal in subsampled images," in *IEEE Statistical Signal Processing Workshop (SSP)*, Palma de Mallorca, Spain, Jun 2016, pp. 1–5.
- [7] I. Smal, E. Meijering, K. Draegestein, N. Galjart, I. Grigoriev, A. Akhmanova, M. Van Royen, A. B. Houtsmuller, and W. Niessen, "Multiple object tracking in molecular bioimaging by rao-blackwellized marginal particle filtering," *Medical Image Analysis*, vol. 12, no. 6, pp. 764–777, Dec 2008.
- [8] I. Smal, W. Niessen, and E. Meijering, "A new detection scheme for multiple object tracking in fluorescence microscopy by joint probabilistic data association filtering," in *IEEE International Symposium on Biomedical Imaging: From Nano to Macro (ISBI)*, Paris, France, May 2008, pp. 264–267.
- [9] D. S. Bright and E. B. Steel, "Two-dimensional top hat filter for extracting spots and spheres from digital images," *Journal of Microscopy*, vol. 146, no. 2, pp. 191–200, May 1987.
- [10] Y. Kimori, N. Baba, and N. Morone, "Extended morphological processing: a practical method for automatic spot detection of biological markers from microscopic images," *BMC bioinformatics*, vol. 11, no. 1, pp. 1–13, July 2010.
- [11] F. He, B. Xiong, C. Sun, and X. Xia, "A laplacian of gaussian-based approach for spot detection in two-dimensional gel electrophoresis images," in *International Conference on Computer and Computing Technologies in Agriculture*. Beijing, China: Springer, Sept. 2010, pp. 8–15.
- [12] S. Seth, A. R. Akram, K. Dhaliwal, and C. K. Williams, "Estimating bacterial and cellular load in fcfm imaging," *Journal of Imaging*, vol. 4, no. 1, pp. 1–11, Jan 2018.
- [13] S. Jiang, X. Zhou, T. Kirchhausen, and S. T. Wong, "Detection of molecular particles in live cells via machine learning," *Cytometry Part A*, vol. 71, no. 8, pp. 563–575, Aug 2007.
- [14] C. Arteta, V. Lempitsky, and A. Zisserman, "Counting in the wild," in *European Conference on Computer Vision (ECCV)*. Amsterdam, The Netherlands: Springer, Oct 2016, pp. 483–498.
- [15] V. Lempitsky and A. Zisserman, "Learning to count objects in images," in *Advances in neural information processing systems*, Dec 2010, pp. 1324–1332.
- [16] N. Ayache, T. Vercauteren, G. Malandain, F. Oberrietter, N. Savoie, and A. Perchant, "Processing and mosaicing of fibered confocal images," in *Medical Image Computing and Computer-Assisted Intervention (MICCAI): Workshop on Microscopic Image Analysis with Applications in Biology (MIAAB)*. Copenhagen, Denmark: Springer, 2006, pp. 1–5, invited. [Online]. Available: <https://hal.inria.fr/inria-00615589>
- [17] G. Le Goualher, A. Perchant, M. Genet, C. Cavé, B. Viellerobe, F. Berier, B. Abrat, and N. Ayache, "Towards optical biopsies with an integrated fibered confocal fluorescence microscope," in *Medical Image Computing and Computer-Assisted Intervention (MICCAI)*. Saint-Malo, Brittany, France: Springer, Sept 2004, pp. 761–768.
- [18] N. Krstajić, A. R. Akram, T. R. Choudhary, N. McDonald, M. G. Tanner, E. Pedretti, P. A. Dalgarno, E. Scholefield, J. M. Girkin, A. Moore *et al.*, "Two-color widefield fluorescence microendoscopy enables multiplexed molecular imaging in the alveolar space of human lung tissue," *Journal of Biomedical Optics*, vol. 21, no. 4, pp. 046 009–046 009, 2016.
- [19] A. K. Eldaly, Y. Altmann, A. Perperidis, N. Krstajic, T. R. Choudhary, K. Dhaliwal, and S. McLaughlin, "Deconvolution and restoration of optical endomicroscopy images," *IEEE Trans. Comput. Imag.*, vol. 4, no. 2, pp. 194–205, March 2018.
- [20] A. K. Eldaly, Y. Altmann, A. Perperidis, and S. McLaughlin, "Deconvolution of irregularly subsampled images," in *IEEE Statistical Signal Processing Workshop (SSP)*, Freiburg, Germany, June 2018, pp. 303–307.
- [21] A. Perperidis, H. E. Parker, A. Karam-Eldaly, Y. Altmann, K. Dhaliwal, R. R. Thomson, M. G. Tanner, and S. McLaughlin, "Characterization and modelling of inter-core coupling in coherent fiber bundles," *Optics Express*, vol. 25, no. 10, pp. 11 932–11 953, May 2017.
- [22] M. V. Afonso, J. M. Bioucas-Dias, and M. A. Figueiredo, "An augmented lagrangian approach to the constrained optimization formulation of imaging inverse problems," *IEEE Trans. on Image Process.*, vol. 20, no. 3, pp. 681–695, March 2011.
- [23] J. Nocedal and S. Wright, *Numerical optimization*. Springer Science & Business Media, 2006.
- [24] P. L. Combettes and V. R. Wajs, "Signal recovery by proximal forward-backward splitting," *Multiscale Modeling & Simulation*, vol. 4, no. 4, pp. 1168–1200, Nov 2005.
- [25] K. Engan, S. O. Aase, and J. H. Husøy, "Multi-frame compression: Theory and design," *Signal Processing*, vol. 80, no. 10, pp. 2121–2140, Oct. 2000.
- [26] M. Aharon, M. Elad, A. Bruckstein *et al.*, "K-svd: An algorithm for designing overcomplete dictionaries for sparse representation," *IEEE Trans. on Signal Process.*, vol. 54, no. 11, p. 4311, Nov 2006.
- [27] O. Mandula, I. Š. Šestak, R. Heintzmann, and C. K. Williams, "Localisation microscopy with quantum dots using non-negative matrix factorisation," *Optics express*, vol. 22, no. 20, pp. 24 594–24 605, Sept. 2014.
- [28] T. Lindeberg, "Feature detection with automatic scale selection," *International journal of computer vision*, vol. 30, no. 2, pp. 79–116, July 1998.